Korean J. Chem. Eng., 39(11), 2935-2944 (2022)
DOI: 10.1007/s11814-022-1213-1

pISSN: 0256-1115
eISSN: 1975-7220

Numerical investigation of the rotating instability uniqueness in a MWe scale supercritical carbon dioxide centrifugal compressor

Zhiyuan Liu*,, Peng Wang***, and Ben Zhao****,†**

*School of Chemical Engineering and Energy Technology, Dongguan University of Technology, Dongguan, China, 5238
**School of Energy and Power Engineering, Xi'an Jiaotong University of Technology, Dongguan, China, 523808
***School of Energy Power and Mechanical Engineering, North China Electric Power University, Beijing, China, 102206
****Institute of Engineering Thermophysics, Chinese Academy of Science, Beijing, China, 100190
(*Received 27 February 2022 • Revised 21 May 2022 • Accepted 21 June 2022*)

Abstract−Flow instability attracts much attention for air compressors but little for a supercritical carbon dioxide (CO_2) compressor that is a critical component in the supercritical CO_2 Brayton cycle. This paper presents a numerical investigation of the rotating instability in a megawatt-scale (MWe-scale) supercritical CO_2 centrifugal compressor from the Institute of Engineering Thermophysics. Unsteady full annulus simulations were carried out at different operating conditions and validated by the experimental data. According to the validated method, we analyzed the blade tip leakage flow, the rotating instability, and the propagation speed of the stalled flow cell. The findings are that (1) the blockage effects of leakage flow are responsible for rotating instability, and (2) the propagation speed of rotating cells is approximately 16.67% of the rotor speed. The novelty is that the figure is lower than that in air compressors, close to that found in water pumps.

Keywords: Supercritical CO_2, Centrifugal Compressor, Rotating Instability, Propagation Speed

INTRODUCTION

Centrifugal compressors are widely used in the energy and power industries, such as refrigeration and turbochargers, because of their reliability and compactness. Rotating stall is a bottleneck issue in centrifugal compressor development and affects its applications in industry. The qualitative understanding of centrifugal compressor stalls has made great progress with the experimental technology and computation fluid dynamics (CFD) development. Frigne and van den Braembussche [1] classified centrifugal compressor stall into three types: vaneless diffuser stall, abrupt impeller stall, and progressive impeller stall. Their experiments found that different types of rotating stall have distinctive characteristics. Thereafter, Haupt et al. [2] discovered rotating stall at the inlet tip zone in a high pressure ratio centrifugal compressor. In addition, Lenneman and Howard [3] carried out experimental studies on an open impeller. The result indicates that the tip clearance vortex is an important factor affecting the impeller operation stability. Mizuki and Oosawa [4] studied the unsteady phenomena in a centrifugal compressor and found that the part-span stall initially appeared at the inlet. However, full-span stall occurred with the compressor mass flow rate reduction. Hoying and Vo et al. [5,6] created the criterion for the spike stall in axial compressors based on unsteady simulations. The investigation shows that the interface between tip leakage flow and main flow is critical in determining whether stall occurs. Yang et al. [7] discovered the same flow phenomenon described as Vo's criterion in a high-speed centrifugal compressor. Schleer et al. [8] found that the trajectory of the leakage vortex is affected by the mass flow rate. The trajectory can be perpendicular to the rotating axis when the flow rate is low enough. The leakage vortex interacts with the adjacent blades, thus forming the inlet tip recirculation.

Kameier et al. [9] observed the unsteady fluctuation at the compressor blade tip. The fluctuation is related to the aerodynamic noise formation of an axial compressor and called rotating instability. Even if the compressor inlet boundary conditions and outlet boundary conditions are steady, the internal flow of the compressor is always unsteady, which means that the internal flow field enters a self-excited fluctuation state. Experiments and simulations found the fluctuation of this sort has a characteristic propagation speed and wavelength in the circumferential direction. Rotating instability is a large-scale unsteady flow phenomenon that occurs before the rotating stall. The physical mechanism is identified as the periodical interaction between the tip leakage vortex and adjacent blades [10]. Since the rotating instability occurs before the rotating stall, it is promising to be a worthy signal for stall warning [11]. Moreover, rotating instability will produce an unsteady exciting force. To avoid resonance, engineers should keep the natural frequency away from the characteristic frequency of rotating instability in the compressor design stage. Finally, if the rotating instability comes from blade tip blockage, a self-circulating casing treatment will be promising to expand the margin of the compressor. This is an incentive to identify the rotating instability signals, the rotating cell number, and propagation speed [12].

Table 1 summarizes the rotating instability characteristics of some compressors and pumps. The cell number is normalized by dividing the blade number. The circumferential propagation speed in

†To whom correspondence should be addressed.
E-mail: 602182622@qq.com

Table 1. Summary of rotating instability characteristics

Fluid	Type	Cells number	Rotating speed	References
Air	Axial	0.31	92.5%	Schreiber et al. [13]
Air	Centrifugal	-	68%	Sun et al. [14]
Air	Centrifugal	-	65.22%	Sun et al. [15]
Air	Axial	0.5	55%	Mailach et al. [16]
Air	Axial	-	52.75	Zhang et al [17]
Air	Axial	0.23	72.2%	Inoue et al. [18]
Air	Centrifugal	0.64	48.2%	Wang et al. [19]
Water	Centrifugal	-	33%	Pavesi et al. [20]
Water*	Centrifugal	0.28-0.57	18-28%	Dazin et al. [21]
Water	Centrifugal	-	25.5%	Krause et al. [22]
Water	Centrifugal	-	6.2%	Sinha et al. [23]

*The value is related to the work flow rate.

the relative coordinate system is normalized by wheel speed. The comparison indicates that the rotating speed of instability cells in air compressors is higher than in water pumps.

Although rotating speeds of the same type of compressors are not constant, it can be seen from Table 1 that the propagation speed of all air compressors is greater than that of all water pumps; thus, the influence of fluid types on the propagation speed is the most important factor. That is, the fluid type plays a dominant role in rotating instability characteristics. Recently, Liu and Sun proved that decreasing fluid compressibility would reduce the rotating speed of instability cells using an eigenvalue method [24].

The supercritical carbon dioxide (CO_2) Brayton cycle was proposed in the 1950s [25], but it did not get much attention at that time. As global energy and environmental problems become serious, the supercritical CO_2 Brayton cycle has received more and more attention in the 21st century [26]. Compression is one of the critical processes in a supercritical CO_2 cycle, greatly influencing both the cycle system performance and stability. As one of the compression devices, the centrifugal compressor has the advantages of high single-stage pressure ratio, flow stability, compactness, cheapness, etc. Our previous research showed that the centrifugal compressor is the most suitable compression component in a 1-100 megawatt (MWe) supercritical CO_2 Brayton cycle power generation system [27,28].

So far, there are few reports about the supercritical CO_2 compressor instability. This paper investigates the rotating instability based on an MW scale supercritical CO_2 compressor. The supercritical CO_2 compressor geometry, the CFD method, and the validation information are introduced in Sections 2 and 3. According to the validated CFD results, the compressor flow field is examined and the flow instability is analyzed in Section 4. Following them, discussion and conclusions are drawn.

INVESTIGATED MODEL

The Institute of Engineering Thermophysics in the Chinese Academy of Sciences (IET-CAS) has conducted experimental research on a megawatt-scale supercritical CO_2 centrifugal compressor and made an effort to address problems such as compressor seal, axial thrust balance, rotor dynamics, and working medium regeneration [29]. A photograph of the compressor impeller tested is shown in Fig. 1.

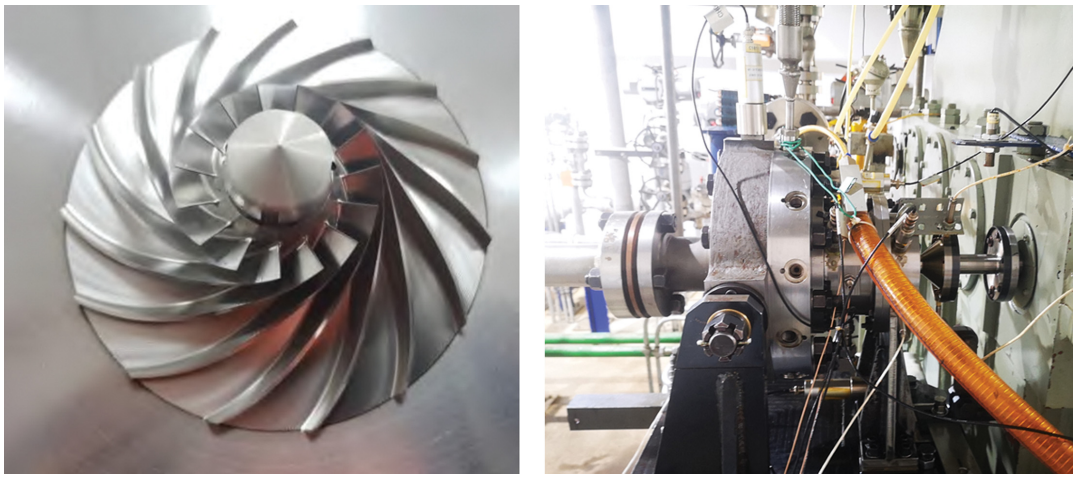

Fig. 1. IET supercritical CO_2 centrifugal impeller (Zhu et al. [29]).

Table 2. Design specification of the IET impeller [29]

Item	Value	Item	Value
Blade number	15	Split blade number	0
Hub diameter	20 mm	Outlet blade height	3.5 mm
Impeller diameter	96 mm	Blade angle at inlet	60°/48°
Inlet blade height	7.5 mm	Blade angle at outlet	50°
Shroud diameter	40 mm	Blade thinness	1.5 mm
Tip clearance	0.45 mm	Reaction degree	0.71

The tested megawatt-scale supercritical CO_2 centrifugal compressor consists of an intake pipe, an impeller, a vaneless diffuser, and a volute. The impeller has 15 blades. Table 2 lists its main geometric parameters.

Compared with the Sandia compressor, the IET compressor employs a vaneless diffuser. The investigated compressor does not have a strong rotor-stator interaction, which is more suitable for the study of impeller rotating instability. The design speed and flow rate of the IET compressor are 40,000 RPM and 16.3 kg/s, respectively. The maximum rotating speed during experimental operations is 34,500 RPM (about 86.25% of the design value) because of some issues caused by the vibration.

COMPUTATIONAL FRAMEWORK

1. Computational Mesh

The simulation domains include the inlet pipe, impeller, vaneless diffuser, and an artificial outlet nozzle, where an entire structured grid is employed, as shown in Fig. 2. The inlet and outlet nozzle are extended appropriately to avoid the boundary condition reflection. The Numeca/IGG package generates the computation mesh of the whole compressor stage. An HO topology pattern is employed for the impeller part. Specifically, an O-type block is used around the blade, and four H-type blocks are applied inside the B2B channel. As for the blade tip clearance, a H-type block surrounded by an O-type block is utilized.

Mesh near the leading edge of the impeller is locally refined by pressing "add Z Constant Line" button of Autogrid software. A mesh independence investigation is performed to eliminate the influence of node number on numerically predicted results, as shown in Fig. 3. It depicts that the grid independence requirement is met when the number of grid nodes is greater than 8.5×10^6. 17 grid points are specified along the span-wise direction inside the tip clearance for the final computational mesh. With a first-layer wall distance of 1.2×10^{-6} m, the maximum y-plus value on all the blade surfaces is below 50, less than the wall function maximum limitation suggested by the NUMECA manual.

2. Numerical Model

The unsteady Reynolds averaged Navier Stokes (URANS) equation is solved by a commercial CFD software Numeca/Fine Turbo. The Span-Wagner model is employed as the equation of state by the Numeca/Tabgen package. The thermodynamic property table ranges were 250-600 K with 501 nodes for temperature and 1-30 MPa with 501 nodes for pressure. The resolution of the physical property table is enough to meet the table independence requirement, according to the investigations of Li et al. [30] and Saxena et al. [31]. The fourth-order explicit Runge-Kutta scheme discretizes the time term in the governing equation. The second-order central difference scheme is adopted for the inviscid flux calculation. The multi-grid strategy and implicit residual smoothing method are used to accelerate convergences. The set of governing equations is presented as follows:

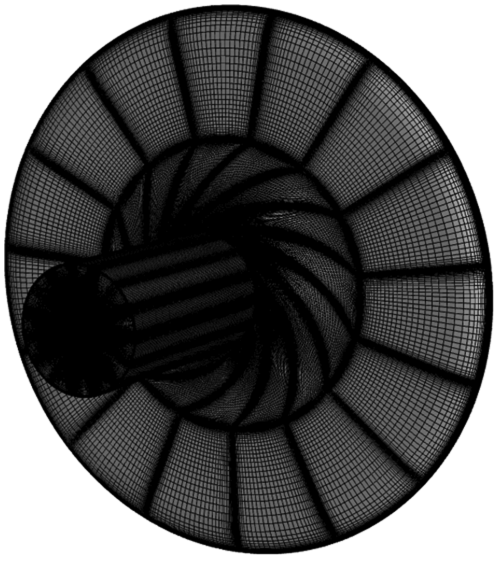

Fig. 2. Grid of the MWe supercritical CO_2 centrifugal compressor.

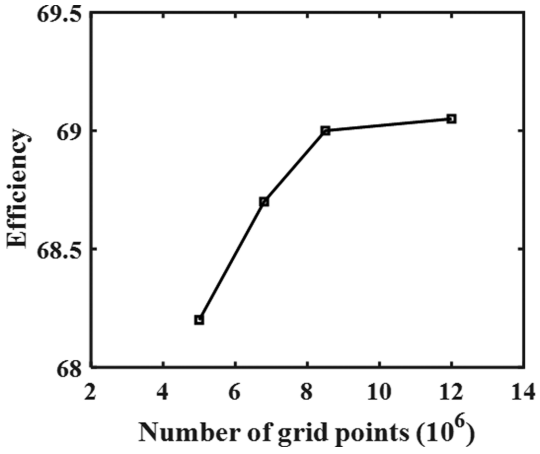

Fig. 3. Grid of the MWe supercritical CO_2 centrifugal compressor.

$$\frac{\partial}{\partial t}\int_{\Omega} U d\Omega + \int_{S} F_i \cdot dS + \int_{S} F_v \cdot dS = \int_{\Omega} S_T d\Omega \tag{1}$$

$$U = \begin{bmatrix} \overline{\rho} \\ \overline{\rho}\tilde{w}_1 \\ \overline{\rho}\tilde{w}_2 \\ \overline{\rho}\tilde{w}_3 \\ \overline{\rho}\tilde{E} \end{bmatrix} \quad F_i = \begin{bmatrix} \overline{\rho}\tilde{w}_i \\ \overline{P^*}\delta_{1i} + \overline{\rho}\tilde{w}_1\tilde{w}_i \\ \overline{P^*}\delta_{2i} + \overline{\rho}\tilde{w}_2\tilde{w}_i \\ \overline{P^*}\delta_{3i} + \overline{\rho}\tilde{w}_3\tilde{w}_i \\ (\overline{\rho}\tilde{E} + \overline{P^*})\tilde{w}_i \end{bmatrix} \quad -F_v = \begin{bmatrix} 0 \\ \overline{\tau}_{i1} \\ \overline{\tau}_{i2} \\ \overline{\tau}_{i3} \\ \overline{q}_i + \tilde{w}_i\overline{\tau}_{ij} \end{bmatrix} \tag{2}$$

$$\tilde{E} = \tilde{e} + \frac{1}{2}\tilde{w}_i\tilde{w}_i + \tilde{k} \tag{3}$$

$$\overline{P^*} = \overline{P} + \frac{2}{3}\overline{\rho}\tilde{k} \tag{4}$$

$$S_T = \begin{bmatrix} 0 \\ (-\overline{\rho})[2w \times w + (w \times (w \times r))] \\ \overline{\rho} w \cdot \nabla(0.5 w^2 r^2) \end{bmatrix} \tag{5}$$

where Ω represents the control volume; S stands for the surface of the control volume; U denotes the conserved quantity, F_i represents the inviscid flux; F_v and S_T stand for the viscous flux and the source term. Mentor's SST turbulence model is utilized to take the turbulence effects into simulation because of its robustness and the ability to deal with complex flows in centrifugal compressors [32].

$$\frac{\partial}{\partial t}(\rho k) + \frac{\partial}{\partial x_i}(\rho k u_i) = \frac{\partial}{\partial x_j}\left(\Gamma_k \frac{\partial k}{\partial x_j}\right) + G_k - Y_k + S_k \tag{6}$$

$$\frac{\partial}{\partial t}(\rho\omega) + \frac{\partial}{\partial x_i}(\rho\omega u_i) = \frac{\partial}{\partial x_j}\left(\Gamma_\omega \frac{\partial \omega}{\partial x_j}\right) + G_\omega - Y_\omega + D_\omega + S_\omega \tag{7}$$

$$\Gamma_k = \mu + \frac{\mu_t}{\sigma_k} \tag{8}$$

$$\Gamma_\omega = \mu + \frac{\mu_t}{\sigma_\omega} \tag{9}$$

For the turbulent diffusion term ($\overline{q}_i$) in the energy equation, the original calculation method of Fine/Turbo is by the temperature gradient and turbulent thermal conductivity, in the form as follows:

$$\overline{q}_i = (\overline{k} + k_t)\frac{\partial \tilde{T}}{\partial x_i} = \left(\overline{k} + \frac{\mu_t}{Pr_t}C_p\right)\frac{\partial \tilde{T}}{\partial x_i} \tag{10}$$

The specific heat capacity at constant pressure may lead to numerical instability when solving the energy equation. To avoid this problem, the calculation method displayed in Eq. (11) is adopted in this work, rather than Eq. (10). The enthalpy-based diffusion term can maintain the residual below 10^{-5}.

$$\overline{q}_i = \overline{k}\frac{\partial \tilde{T}}{\partial x_i} - \overline{\rho w_i'' h''} = \overline{k}\frac{\partial \tilde{T}}{\partial x_i} + \frac{\mu_t}{Pr_t}\frac{\partial \tilde{h}}{\partial x_i} \tag{11}$$

Table 3. Validation case operating condition

T_0	P_0	α	N
309.4 K	7.827 MPa	0°	34,500 RPM

3. Boundary Conditions

The total temperature and total pressure are specified at the inlet boundary of the computational mesh, as illustrated in Table 3. It is assumed that there is no pre-swirl at the inlet boundary. At the outlet boundary, the average static pressure is specified. The multiple operation points are obtained by gradually raising the static pressure at the outlet boundary. All the wall surfaces except for the artificial nozzle, the adiabatic condition, and a mean roughness of 1.6 μm are defined. Walls inside conventional air compressors are hydraulically smooth, and the influence of roughness can usually be ignored. However, for supercritical CO_2 compressors, walls are hydraulically rough. The surface roughness, therefore, has effects on compressor aerodynamic performance. The slip boundary condition is set as the artificial nozzle is used in the downstream region. The nozzle used can enhance the convergence near the stall point.

The complete computational domain is solved in the rotating frame of reference. Therefore, the vaneless diffuser hub has a counter rotating speed. To capture the characteristics of high-frequency unsteady flow field at the near stall condition, the physical time step in unsteady simulation is one-twentieth of the impeller turning

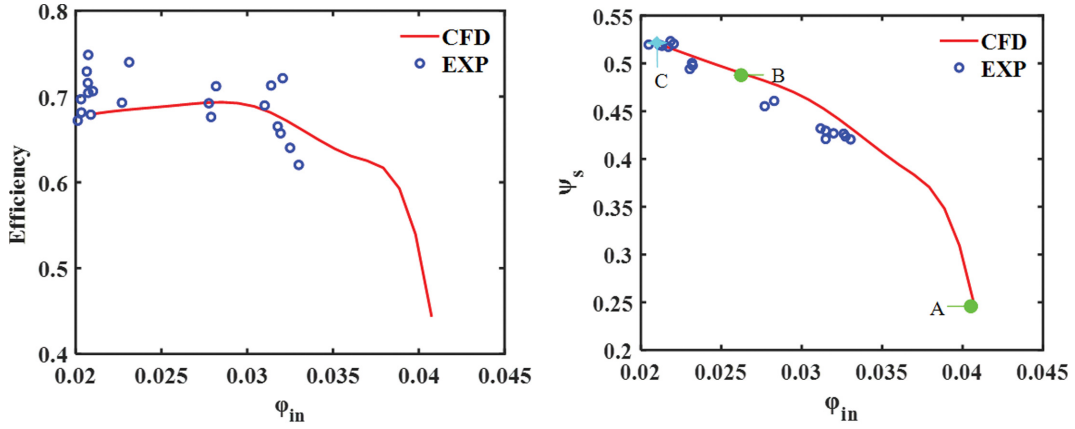

(a) Actual efficiency (b) Work coefficient

Fig. 4. Comparison between URANS simulations and experiment.

Table 4. Comparison of CFD and experimental results near stall condition

Items	EXP	URANS	Deviation
Stall flow rate	8.274 kg/s	8.174 kg/s	1.21%
Corresponding pressure ratio	1.782	1.763	1.07%
Corresponding efficiency	0.68-0.77	0.68	N/A

one blade channel, i.e., the time step is 5.8×10^{-6} s. Each physical time step adopts 30 internal time steps to ensure convergence. The unsteady simulations are expensive in CUP time and computation resources and are adopted only for the near stall condition. As for other operation points, steady simulations are employed.

During the IET MWe supercritical CO_2 centrifugal compressor test, the stall condition is determined by monitoring the amplitude of shaft vibration. When the amplitude exceeds 300 μm, the compressor operating point is identified as stall onset. Fig. 4(a) and Fig. 4(b) describe the compressor efficiency and work coefficient as a function of the flow coefficient, respectively. The definitions of the flow coefficient, actual efficiency, and work coefficient are introduced in Eqs. (12)-(14). To account for the effect of volute, the compressor performance is revised with the Aungier loss model [33].

$$\varphi_{in}=\frac{\dot{V}_0}{\frac{1}{4}\pi D_2^2 U_2}=\frac{4\dot{m}}{\pi\rho_0 D_2^2 U_2} \tag{12}$$

$$\eta_{ac}=\frac{M\omega\eta-\Delta h_{volute}}{M\omega} \tag{13}$$

$$\psi_s=\frac{\Delta h_s}{U_2^2}=\frac{M\omega\eta_{ac}}{\dot{m}U_2^2} \tag{14}$$

The deviation between the CFD and experimental results should be acceptable as far as the compressor efficiency and the fluid enthalpy rise. The good agreement gives confidence to the numerical simulation method.

The aerodynamic characteristics under near stall conditions are the focus of this paper. Table 4 illustrates the comparison between the main parameters of the near stall condition and corresponding numerical results. The agreement in compressor near stall prediction also gives the RANS and URANS simulations confidence.

Table 5. Comparison of CFD and experimental results near stall condition

Items	A	B	C
Flow coefficient	0.041	0.026	0.021
Work coefficient	0.246	0.493	0.521
Actual efficiency	0.443	0.69	0.68

Three operation conditions (A, B, and C) are selected to investigate the influence of the load coefficient on the internal flow of the compressor: near choke, maximum efficiency, and near stall conditions, respectively. Table 5 displays the performance of three states. The detailed examination of the compressor flow field will be discussed in Section 4.

ROTATING INSTABILITY ANALYSIS

1. Blockage Effect of Leakage Flow

The axial momentum variation of leakage flow and mainstream are the main factors that induce rotating instability and rotating stall [34]. The interface between the leakage flow and the mainstream can be used to indicate the momentum ratio, according to [35]. Fig. 5 compares the distribution of the circumferential average entropy at the meridional plane. Since the leakage flow is formed by a rapid contraction and expansion process through the tip clearance, it has much higher entropy than the mainstream. Therefore,

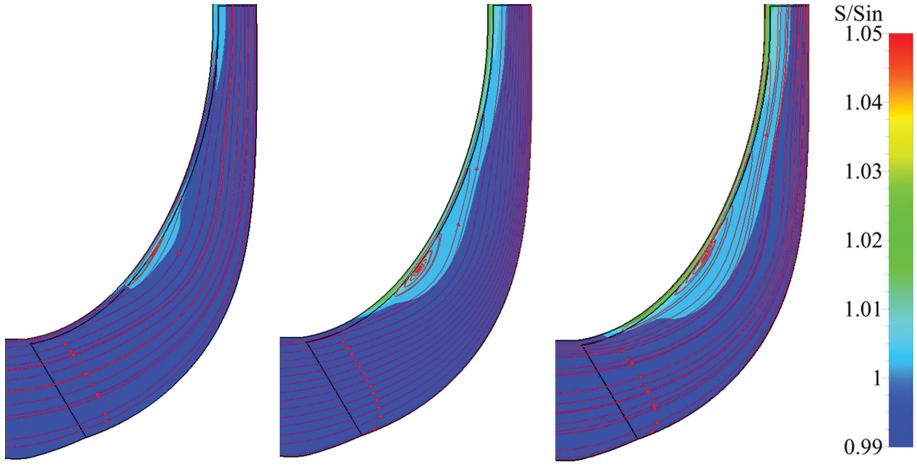

(a) Condition A (b) Condition B (c) Condition C

Fig. 5. Circumferential average entropy distribution of the three operation conditions.

a high entropy value at the tip region indicates the position has strong leakage flow or blockage. Under the choke condition, the high entropy area is distributed only at the tip area in the middle of the impeller. As the flow coefficient decreases to condition B, the leakage flow has been greatly expanded in the meridional and the spanwise directions because of the leakage flow momentum enhancement. As a result, the interface moves towards the leading edge and hub. After further development, the interface between the leakage flow and the mainstream is close to the leading edge at the near stall condition (C). The interface change is closely related to the blockage effect occurring in impeller channels and the stall inception.

The blockage factor can reveal the intensity of the blockage effect caused by the recirculation zone. According to Ghenaiet and Khalfallah [36], the sudden increase of blockage factor can be used for the compressor stall criterion. The boundary between the blockage region and mainstream region refers to the method of Garrison and Cooper [37] and is distinguished by the density-flow gradient. On the quasi-S3 flow surface, the density-flow gradient is the vector sum of spanwise and circumferential gradients, and the following formula can calculate its magnitude:

$$\nabla(\rho W_m)=\sqrt{\left(\frac{\partial(\rho W_m)}{\partial r}\right)^2+\left(\frac{\partial(\rho W_m)}{\partial t}\right)^2} \tag{15}$$

where, r stands for the spanwise direction and t represents the circumferential direction. The reference [38] defines the region where the local density-flow gradient is greater than the average local density-flow gradient as the blockage area and the other as the core area. Coupled with the above methods, Fig. 6 displays the location and size of the blockage area near the leading edge section (Z= 0.002 m) of the MWe supercritical CO_2 centrifugal compressor under different flow rates.

As outlined in Fig. 6, under the choke condition, the blockage area is mainly concentrated in the blade boundary layer and the shroud-blade corner. When the impeller flow rate reduces to the operating point of B, the blockage region has the same location, but its area increases slightly. While, under the near stall condition, the shroud-blade corner blockage increases significantly and represents a sudden expansion of the blockage, thus indicating an instability

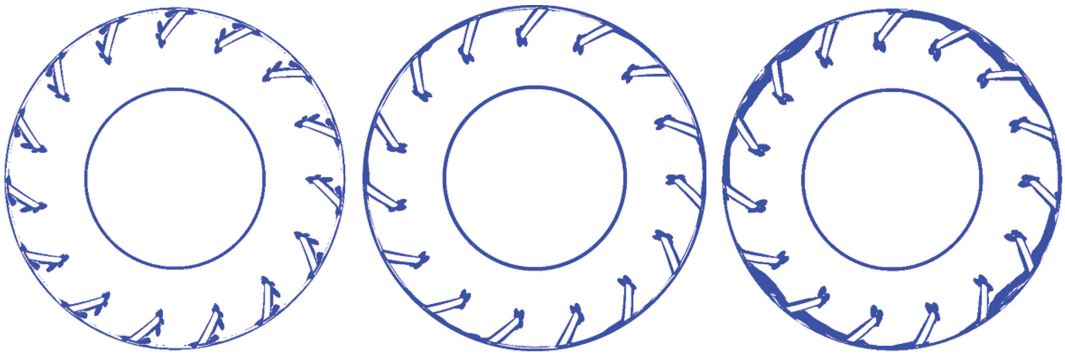

(a) Condition A (b) Condition B (c) Condition C

Fig. 6. Blockage distribution at the inlet of the MWe supercritical CO_2 compressor.

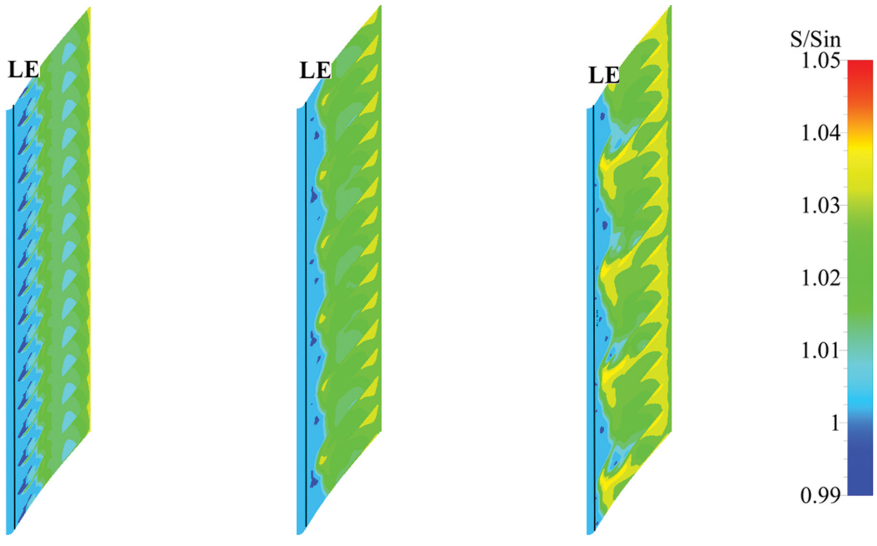

(a) Condition A (b) Condition B (c) Condition C

Fig. 7. Tip entropy distribution of the MWe supercritical CO_2 centrifugal compressor.

onset.

Fig. 7 compares the dimensionless entropy at 98% span of the supercritical CO_2 centrifugal impeller. Under the choke condition (A), the high entropy region is located at the rear end of impeller and no significant difference can be seen in each blade channel. When the flow coefficient goes down to 0.026 (condition B), the high entropy region expands, and the entropy interface moves forward to the blade leading edge (LE). Moreover, the vital discrepancy from the choke condition is the flow image in each blade channel is no longer the same. IOW, the period number in the circumferential direction is no longer equal to the blade number. Under condition B, six waves can be identified in the circumferential direction. With the further reduction of the flow coefficient to the near stall condition (C), the interfaces between the leakage flow and the main flow in some blade channels are parallel to the impeller leading edge. According to the stall criterion proposed by Vo et al. [6], the flow in these channels should be unstable. The number of low-energy cells has been reduced to four, similar to the finding of Dazin's study [21]. Consequently, the leakage flow dominant region extends to the whole circumference and contributes to a more significant blockage effect.

2. Leakage Flow Structure at Near Stall Condition

The strike of leakage flow on the adjacent blade pressure surface is one of the necessary conditions to induce rotating instability [39]. Fig. 8 shows the leakage flow structure in the supercritical CO_2 centrifugal impeller. According to flow characteristics, the leakage flow can be divided into parts I, II, and III from upstream to downstream. The corresponding leakage location can be divided into three sections (a, b, and c).

Section a originates from the leading edge and ends at the impeller passage throat, in which the core of the leakage vortex generates. The angle between the leakage vortex and the axial direction is typical. The leakage flow existence in Section a causes a slight blockage in the blade channel.

Section b closely follows Section a and is located around the impeller passage throat. The leakage flow from the tip gas in Section b is entrained by the upstream one, thus increasing the size of the leakage flow region. As a result, the leakage vortex occupies more span in radius and enhances the blockage effect. The enhanced blockage effect further induces the downstream leakage flow (produced in Section c) to have strong inverse momentum. The part of leakage flow having inverse momentum is the main part of secondary leakage flow.

The propagation process of low-energy flow is plotted in Fig. 9 within one period to understand the unsteady evolution process around the blade tip. Fig. 9(a) illustrates the dimensionless entropy distribution at four moments at 90% span. A low-energy cell can influence four blade channels, contributing to the significant difference in entropy between the adjacent blade channels. It moves in the opposite direction in the rotating frame with the impeller rotation. Specifically, at the 0/4T moment, the entropy is higher in the first channel (C1) but lower in the third (C3)and fourth (C4) channels. After 1/4T, the high entropy region occurs in the second channel (C2), followed by low entropy regions in the fourth and fifth channels. The entropy magnitude is an index to reveal the intensity of leakage flow in both the mixing and the blockage effect.

Fig. 9(b) illustrates the static pressure distribution with isolines. At 0/4T, a high-pressure region occurs around the leading edge on the pressure side in the C1 channel. Its formation is attributed to the blockage effect of the leakage flow. The high entropy region of Channel1 and Channel2 represents the leakage vortex originating from the tips of Blade1 and Blade2 and reveals a strong blockage effect. The blockage effect changes the pressure distribution and

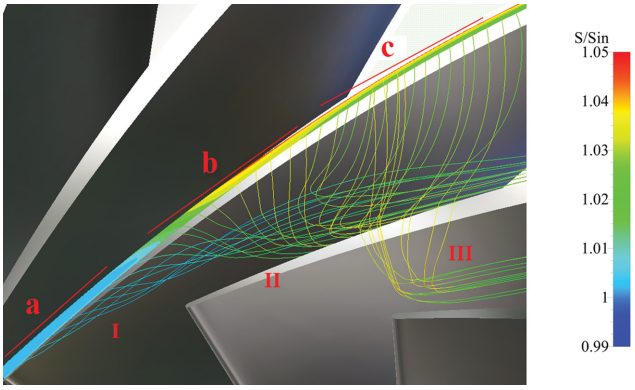

Fig. 8. Structure of tip leakage flow inside the supercritical CO_2 centrifugal impeller.

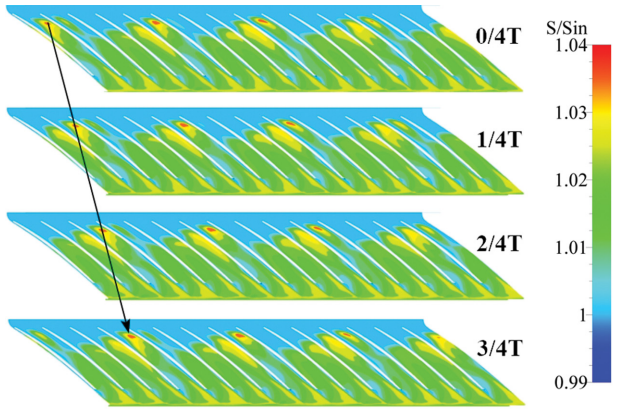

(a) Dimensionless entropy distribution

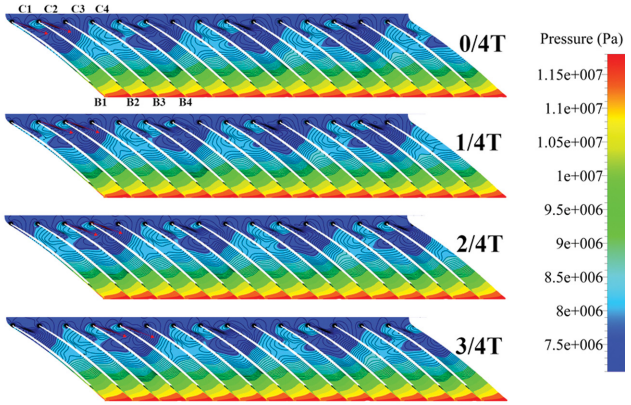

(b) Static pressure distribution

Fig. 9. Dimensionless entropy and pressure distribution at the 90% span.

forms a pressure wave in a local region. The local pressure wave propagates upstream, thus redistributing the inflow condition. The changed inflow affects the subsequent blades by varying the incidence angle, and then induces pressure disturbance in other channels, as shown in Fig. 9(b). The changed pressure distribution results in various leakage flows because the pressure difference between blade sides is the driving force fluid to cross the blade tip gaps, contributing to the different blockage effects. Under the action of the coupling impacts, the impeller has four low-energy cells, as shown in Fig. 9. Both the upstream propagation and the returning impact need time, making the distorted flow field propagate in the contra-rotating direction in the relative rotating frame.

3. Rotating Speed of Stalled Flow Cell

The rotating speed of low-energy cells is an important parameter that can be a theoretical basis for the stall warning of a supercritical CO_2 centrifugal compressor. It has been intensively investigated in air compressors. However, it is not clear whether the conclusion based on an air compressor is fully available for a supercritical CO_2 centrifugal compressor. There is a lack of understanding of the rotating instability in a supercritical CO_2 compressor.

Fifteen numerical probes are located in front of the impeller leading edge to monitor the static pressure. Fig. 10 depicts the probe's location in the meridional plane. Based on the pressure data obtained, it is possible to understand the transient flow characteristics in the supercritical CO_2 centrifugal compressor when the rotating instability occurs. Numerical probes are located in the relative coordinate system and then make it possible to reveal the pressure disturbance information, such as the propagation speed and the amplitude.

Fig. 11 depicts the static pressure signals from three adjacent probes. The pressure signals reveal the similar fluctuation period, waveform, and amplitude as well as an apparent delay in phase. Fig. 12 shows the FFT result of the pressure signal from probe 1. The RF and RIF denote the rotation frequency and rotating instability frequency, respectively. The dominant frequency of rotating instability is 383.3 Hz in the relative frame. Other harmonic frequencies are also identified, consistent with the prediction theory of Holste et al. [40].

The rotating speed of the rotating instability is a function of the dominant frequency value, cells number, and rotation frequency (RF), as described by Eq. (16). The equation figures out a speed in a dimensionless formation. The propagation speed of rotating instability in the circumferential direction is 16.67% of rotor speed for the investigated compressor.

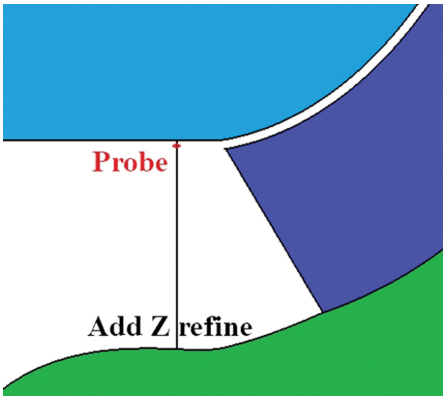

Fig. 10. The position of a probe in the meridional plane.

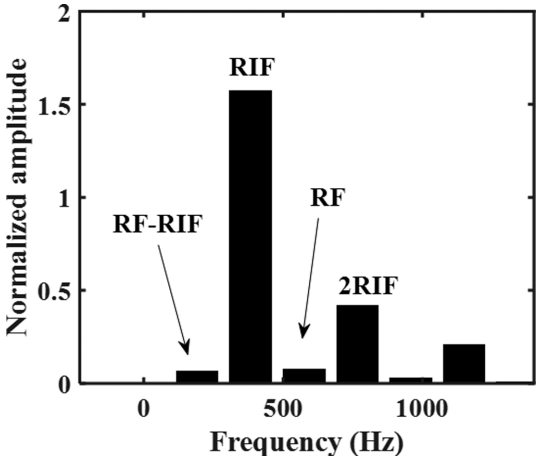

Fig. 12. FFT result of condition C.

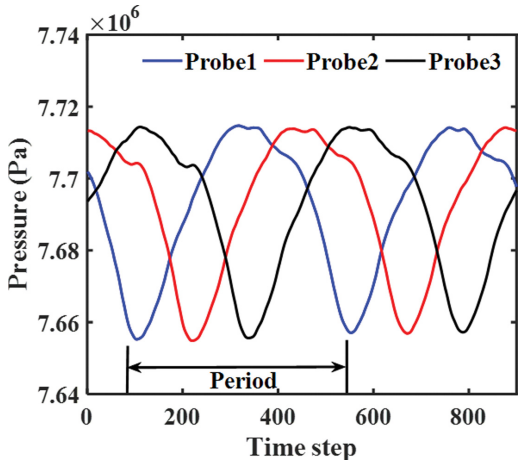

Fig. 11. Pressure signal of three adjacent probes.

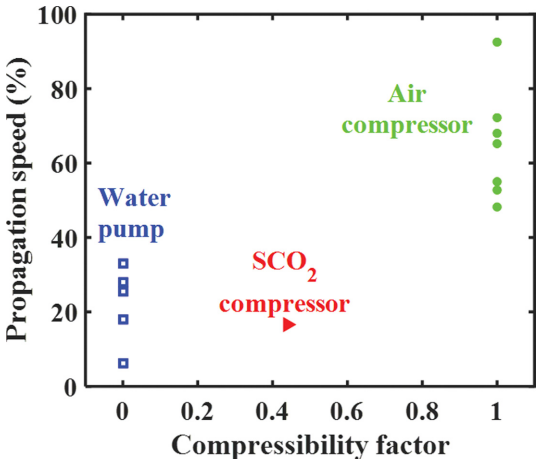

Fig. 13. Instability propagation speed summary.

$$\text{Speed} = \frac{\text{RIF}}{\text{N(cells)} \cdot \text{RF}} = \frac{383.3\ \text{Hz}}{4 \times 575\ \text{Hz}} = 16.67\% \quad (16)$$

The obtained propagation speed of the supercritical CO_2 compressor is significantly different from available air compressor data. The speed should be related to the real gas properties of supercritical CO_2. The non-ideal compressible effects can be described by the compressibility factor (Z). Therefore, Fig. 13 compares the propagation speed of the rotating instability according to the compressibility factors (data from Table 1). For a water pump, $Z \approx 0.001$ while $Z \approx 1$ for an air compressor. The compressibility factor of supercritical CO_2 at the compressor inlet is about 0.44. The propagation speed observed in water pumps is much lower than in air compressors. The novel finding is that the cell propagation speed in a supersonic CO_2 compressor is quite distinct from air compressors but within the speed scope of a water pump.

CONCLUSIONS

This work studied the rotating instability characteristics in the IET MWe supercritical CO_2 compressor by unsteady numerical simulations of the full annulus. The operating point for the rotating instability onset was consistent with the experimental result. The numerical analysis confirms the distinction in the rotating cell propagation speed from air compressors for the first time. The results are summarized as follows:

(1) At the near stall operation point, a sudden expansion of the blockage region makes the interfaces between the leakage flow and the main flow in some blade channels seem to be parallel to the impeller leading edge. Similar to an air compressor, the interface location can be an indicator for the rotating instability onset.

(2) The blockage effect of the tip leakage flow can induce the circumferential rotating pressure wave. Accompanied by the wave, a low-energy cell occurs and occupies four blade channels, resulting in different mixing intensities and blockage factors between adjacent blade channels. It is consistent with the conclusions of air compressors.

(3) The novel finding is that the stable circumferential propagation speed of the low-energy cells is about 16.67% of the rotational speed of the impeller. The figure is lower than the available air compressor data but within the scope of water pump data. The distinction from air compressors should be related to the compressibility of supercritical CO_2.

ACKNOWLEDGEMENTS

This work is financially supported by the National Natural Science Foundation of China (Grant No. 52006217). The authors would like to thank Prof. Yuyan Jiang (now in Beijing Institute of Technology) and Dr. Yuming Zhu from the Institute of Engineering Thermophysics-Chinese Academy of Sciences for sharing their measurement data.

DECLARATION OF CONFLICTING OF INTEREST

The author(s) declared no potential conflicts of interest with respect to the research, authorship, and/or publication of this article.

NOMENCLATURE

D : diameter
E : total energy
F : flux variable
h : specific enthalpy
k : turbulent kinetic energy, heat conductivity
$\dot{m}$: mass flow rate
M : torque
N : shaft speed
P : pressure
Pr : Prandtl number
$\overline{q}_i$: turbulent diffusion term
r : radius
R : gas constant
S : source term, specific entropy
t : circumferential direction
T : temperature
U : conservation variable
w : relative velocity
Z : axial position

Greek Symbols

α : flow angle
ρ : density
φ : flow coefficient
ω : angular velocity, turbulence frequency
μ : dynamic viscosity
τ : viscous stresses tensor

Subscripts

0 : stagnation condition in absolute coordinate
1 : impeller inlet
2 : impeller outlet
s : isentropic process
ac : actual parameter
m : meridional direction
r : radial direction
t : turbulent parameter, tangential direction

Abbreviation

RF : rotation frequency
RIF : rotating instability frequency

REFERENCES

1. P. Frigne and R. Van Den Braembussche, *J. Eng. Gas Turbines Power*, **106**, 468 (1984).
2. U. Haupt, K. Bammert and M. Rautenberg, *Proceedings of the ASME 1985 International Gas Turbine Conference and Exhibit*, **4**, V004T13A007 (1985).
3. E. Lennemann and J. H. G. Howard, *J. Eng. Power*, **92**, 65 (1970).
4. S. Mizuki and Y. Oosawa, *J. Turbomach*, **114**, 312 (1992).
5. D. A. Hoying, C. S. Tan, H. D. Vo and E. M. Greitzer, *J. Turbomach*.,

121, 735 (1999).
6. H. D. Vo, C. S. Tan and E. M Greitzer, *J. Turbomach.*, **130**, 011023 (2008).
7. C. Yang, Y. Wang, D. Lao, D. Tong, L. Wei and Y. Liu, *J. Therm. Sci.*, **25**, 312 (2016).
8. M. Schleer and R. S. Abhari, *J. Turbomach.*, **130**, 031009 (2008).
9. F. Kameier and W. Neise, *J. Sound. Vib.*, **203**, 833 (1997).
10. J. Du, F. Lin, H. Zhang and J. Chen, *J. Turbomach.*, **132**, 021017 (2010).
11. J. Li, S. Geng, J. Du, H. Zhang and C. Nie, *Aerosp. Sci. Technol.*, **85**, 529 (2019).
12. Z. Liu, Q. Zhao, X. Xiang, W. Zhao and X. Zhou, *P. I. Mech. Eng A-J Pow.*, **235**, 335 (2021).
13. J. Schreiber, B. Paoletti and X. Ottavy, *Int. J. Rotating Mach.*, **2017**, 7035870 (2017).
14. X. Sun, Y. Ma, X. Liu and D. Sun, *AIAA J.*, **54**, 2361 (2016).
15. Z. Sun, W. Zou and X. Zheng, *Aerosp. Sci. Technol.*, **82**, 628 (2018).
16. M. Inoue, M. Kuroumaru, S. Yoshida, T. Minami, K. Yamada and M. Furukawa, *Proceedings of the ASME Turbo Expo 2004: Power for Land, Sea, and Air*, **5**, 385 (2004).
17. R. Mailach, I. Lehmann and K. T. Vogeler, *J. Turbomach.*, **123**, 453 (2001).
18. W. Wang, C. Yang, C. Hu and H. Zhang, *P. I. Mech. Eng. D-J Aut*, **236**, 621 (2022).
19. H. Zhang, X. Deng, J. Chen and W. Huang, *J. Therm. Sci.*, **14**, 211 (2005).
20. G. Pavesi, G. Ardizzon and G. Cavazzini, *Proceedings of the ASME 2005 International Mechanical Engineering Congress and Exposition. Fluids Engineering*, **2005**, 67 (2005).
21. A. Dazin, O. Coutier-Delgosha, P. Dupont, S. Coudert, G. Caignaert and G. Bois, *J. Therm. Sci.*, **17**, 368 (2008).
22. N. Krause, K. Zähringer and E. Pap, *Exp. Fluids*, **39**, 192 (2005).
23. M. Sinha, A. Pinarbasi and J. Katz, *J. Fluids Eng.*, **123**, 490 (2001).
24. X. Liu, D. Sun and X. Sun, *J. Fluids Eng.*, **136**, 031102 (2014).
25. E. G. Feher, *Energy Convers.*, **8**, 85 (1968).
26. V. Dostal, M. J. Driscoll, P. Hejzlar and N. E. Todreas, *Proceedings of the 10th International Conference on Nuclear Engineering. 10th International Conference on Nuclear Engineering*, **2**, 567 (2002).
27. Z. Liu, W. Luo, Q. Zhao, W. Zhao and J. Xu, *Appl. Sci.-Basel*, **8**, 595 (2018).
28. Z. Liu, P. Wang, X. Sun and B. Zhao, *Energy*, **240**, 122792 (2022).
29. Y. Zhu, *Study on supercritical carbon dioxide centrifugal compressor*, University of Chinese Academy of Sciences, China, doctoral dissertation (2020).
30. X. Li, Y. Zhao, H. Yao, M. Zhao and Z. Liu, *Energies*, **13**, 5049 (2020).
31. S. Saxena, R. Mallina, F. Moraga and D. Hofer, *Proceedings of the ASME Turbo Expo 2017: Turbomachinery Technical Conference and Exposition*, **9**, V009T38A005 (2017).
32. F. R. Menter, M. Kuntz and R. Langtry, *Heat Mass Transfer*, **4**, 625 (2003).
33. R. H. Aungier, *Centrifugal compressors: A strategy for aerodynamic design and analysis*, American Society of Mechanical Engineers Press, New York (1999).
34. J. Du, Y. Li, Z. Li, J. Li, Z. Wang and H. Zhang, *Energy*, **172**, 618 (2019).
35. J. D. Cameron, M. A. Bennington, M. H. Ross, S. C. Morris, J. Du, F. Lin and J. Chen, *J. Turbomach.*, **135**, 051005 (2013).
36. A. Ghenaiet and S. Khalfallah, *Aerosp. Sci. Technol.*, **88**, 193 (2019).
37. S. A. Khalid, A. S. Khalsa, I. A. Waitz, C. S. Tan, E. M. Greitzer, N. A. Cumpsty, J. J. Adamczyk and F. E. Marble, *Proceedings of the ASME 1998 International Gas Turbine and Aeroengine Congress and Exhibition*, **1**, V001T01A047 (1998).
38. Z. Li, X. Lu, G. Han, Y. Zhang, S. Zhao and J. Zhu, *P I MECH ENG A-J POW.*, **234**, 156 (2020).
39. J. Du, F. Lin, H. Zhang and J. Chen, *J. Turbomach.*, **132**, 021017 (2010).
40. F. Holste and W. Neise, *J. Sound Vib.*, **203**, 641 (1997).